Induced excitations in some metal oxides

Sirbu, Silviu

Chapter 3

Terahertz Time-Domain Spectroscopy

3.1 Principles of Terahertz Time-Domain Spectroscopy

In this section we will depict the fundamental physics involved in generation and detection of short-lived transients in nonlinear optical crystals, which is one of the main concepts of this Thesis.

We will start from the Maxwell equations for vacuum and for media and arrive at the wave equation. Finding the solution for the wave equation will give us an important result: the far-field temporal shape of an electromagnetic transient induced by two time-varying sources - polarization and conduction current.

In a second step we will investigate the linear and nonlinear contributions to the optically - induced polarization, and discuss two very important effects in nonlinear optics: optical rectification and second harmonic generation. Optical rectification of ultrashort laser pulses in nonlinear crystals will be employed in this work to generate the THz electromagnetic transients.

Finally, we will describe the linear electrooptic effect in nonlinear crystals, and the phase retardation of the incident optical electromagnetic wave induced by it. This effect will be used in the detection of THz transients by means of the time-resolved optical probing of the electrooptic effect induced by the THz electric field in the nonlinear crystal.

3.1.1 Maxwell's equations. Wave equation and its solution in the far field

Electromagnetic phenomena obey Maxwell's equations. Throughout this section characters written in bold represent vectors, while characters not written in bold represent scalars. In vacuum they can be written in the form

$$\nabla \cdot \mathbf{E} = \frac{\rho}{\varepsilon_0}, \tag{3.1}$$

$$\nabla \times \mathbf{E} = -\frac{\partial \mathbf{B}}{\partial t}, \tag{3.2}$$

$$\nabla \cdot \mathbf{B} = 0, \tag{3.3}$$

$$\nabla \times \mathbf{B} = \mu_0 \varepsilon_0 \frac{\partial \mathbf{E}}{\partial t} + \mu_0 \mathbf{J}, \tag{3.4}$$

where $\mathbf{E}$ is the electric field strength, $\mathbf{B}$ the magnetic induction, $\mathbf{J}$ the current density, ρ the charge density, μ_0 is the magnetic permeability of vacuum, ε_0 electric permittivity of vacuum, and t the time. μ_0 and ε_0 can be related to the speed of light in vacuum, c, through the relation $c = \sqrt{\mu_0 \varepsilon_0}^{-1}$. $\mathbf{E}$, $\mathbf{B}$, and $\mathbf{J}$ are vectors. Taking the time derivative of eq. (3.1) and the divergence of eq. (3.4) one can obtain the continuity equation

$$\frac{\partial \rho}{\partial t} = -\nabla \cdot \mathbf{J} \tag{3.5}$$

In a certain medium, the charge density ρ can be written as a sum of the external charged density ρ_{ext}), and the polarization charge density ρ_{pol}, ρ=$\rho_{ext} + \rho_{pol}$. ρ_{pol} can be related to the polarization density $\mathbf{P}$ through

$$\rho_{pol} = -\nabla \cdot \mathbf{P} \tag{3.6}$$

The sum of the conduction $\mathbf{J}_{cond}$ and displacement $\mathbf{J}_{disp}$ current densities give the total current $\mathbf{J} = \mathbf{J}_{cond} + \mathbf{J}_{disp}$. The displacement current $\mathbf{J}_{disp}$ is related to the polarization density $\mathbf{P}$ by

$$\mathbf{J}_{disp} = \frac{\partial \mathbf{P}}{\partial t} \tag{3.7}$$

The material related parameters are the electric displacement $\mathbf{D}$ and magnetic field strength $\mathbf{H}$, which for a linear isotropic nonmagnetic dielectric are given by

$$\mathbf{D} = \varepsilon \mathbf{E} = \varepsilon_0 \mathbf{E} + \mathbf{P} = \varepsilon_0 (1 + \chi) E \tag{3.8}$$

$$\mathbf{H} = \frac{\mathbf{B}}{\mu_0} \tag{3.9}$$

where ε stands for the dielectric function and χ is the dielectric susceptibility. Then, the polarization density can be expressed by the following relation

$$\mathbf{P} = (\varepsilon - 1)\varepsilon_0 \mathbf{E} = \varepsilon_0 \chi \mathbf{E} \tag{3.10}$$

Taking into account the material parameters and eqs. (3.5) to (3.9), Maxwell's equations can be rewritten as

$$\nabla \cdot \mathbf{D} = \rho_{ext}, \tag{3.11}$$

$$\nabla \times \mathbf{E} = -\frac{\partial \mathbf{B}}{\partial t}, \tag{3.12}$$

$$\nabla \cdot \mathbf{B} = 0, \tag{3.13}$$

$$\nabla \times \mathbf{H} = \mathbf{J}_{cond} + \varepsilon_0 \frac{\partial \mathbf{D}}{\partial t} \tag{3.14}$$

Equations (3.11) until (3.14) are called material Maxwell's equations. The interesting parameters in these equations are the conduction current $\mathbf{J}_{cond}$ and the polarization $\mathbf{P}$ which is included into the displacement $\mathbf{D}$. These parameters are describing the response of the medium to the electromagnetic field. In the absence of free charges, Maxwell's material equations can be combined into a single equation

$$\nabla^2 \mathbf{E} - \frac{1}{c^2} \frac{\partial^2 \mathbf{E}}{\partial t^2} = \mu_0 \left(\frac{\partial \mathbf{J}_{cond}}{\partial t} + \frac{\partial^2 \mathbf{P}}{\partial t^2} \right) \tag{3.15}$$

which describes the propagation of an electromagnetic wave, therefore being called the wave equation. Our interest is to find out the far-field on-axis solution of the wave equation (3.15), which will express the electromagnetic signal on an axis normal to a slab of material and at a substantial distance, emitted by the slab of material with a time-varying spatially uniform conduction current $\mathbf{J}_{cond}$ and/or polarization density $\mathbf{P}$. This solution has been calculated by different authors [1, 2] and has the form

$$\mathbf{E}_{rad}(t) \approx -\frac{\mu_0}{4\pi} \frac{S}{z} \left(\frac{\partial \mathbf{J}_{cond}}{\partial t} + \frac{\partial^2 \mathbf{P}}{\partial t^2} \right) \tag{3.16}$$

where S is the emitting area, and z stands for the distance between the emitter surface and the detection point. This solution allows to reconstruct the polarization and the carrier dynamics in an electromagnetic signal emitter, making the assumption that the radiated field is properly detected.

3.1.2 Linear and nonlinear contributions to polarization

Considering eq. (3.10) in the linear case, the polarization P can be expressed in the form

$$P(r,t) = \int_{-\infty}^{+\infty} \chi^{(1)}(r - r', t - t') E(r', t') dr' dt' \tag{3.17}$$

where $\chi^{(1)}$ is linear susceptibility and a 2^{nd} rank tensor. Considering the electric field a monochromatic plane wave

$$E(r,t) = E(k,\omega) = E_0(k,\omega)exp(ikr - i\omega t) \tag{3.18}$$

where r is the coordinate, k is the wavevector, ω the angular frequency, and E_0 is electric field amplitude. Defining the Fourier transform $\chi^{(1)}(k,\omega) = \int \chi^{(1)}(r-r', t-t')e^{ikr'-i\omega t'}dr'dt'$, the k and ω dependent polarization can be written as

$$P(r,t) = P(k,\omega) = \chi^{(1)}(k,\omega)E_0(k,\omega) \tag{3.19}$$

and the dielectric function

$$\varepsilon(k,\omega) = 1 + \frac{\chi^{(1)}(k,\omega)}{\varepsilon_0} \tag{3.20}$$

In the nonlinear case the polarization can be expanded into a powers series of E as following

$$\begin{aligned} P(r,t) = &\int_{-\infty}^{+\infty} \chi^{(1)}(r-r', t-t')E(r',t')dr'dt' + \\ &\int_{-\infty}^{+\infty} \chi^{(2)}(r-r_1, t-t_1; r-r_2, t-t_2) \\ &\times E(r_1,t_1)E(r_2t_2)dr_1dt_1dr_2dt_2 + ... \end{aligned} \tag{3.21}$$

where $\chi^{(i)}$ stands for the i-th order nonlinear susceptibility and is a tensor of (1+i)th rank. Now the k and ω dependent polarization can be written as

$$P(k,\omega) = P^{(1)}(k,\omega) + P^{(2)}(k,\omega) + P^{(3)}(k,\omega) + ... \tag{3.22}$$

with

$$\begin{aligned} &P^{(1)}(k,\omega) = \chi^{(1)}(k,\omega)E(k,\omega) \\ &P^{(2)}(k,\omega) = \chi^{(2)}(k = k_i + k_j, \omega = \omega_i + \omega_j)E(k_i,\omega_i)E(k_j\omega_j) \\ &P^{(3)}(k,\omega) = \chi^{(3)}(k = k_i + k_j + k_k, \omega = \omega_i + \omega_j + \omega_k) \times E(k_i,\omega_i)E(k_j,\omega_j)E(k_k,\omega_k) \end{aligned} \tag{3.23}$$

The last equation shows clearly that nonlinear susceptibilities of the order higher then 1 provide mixing frequencies of the different monochromatic waves, if their wavevectors match (phase matching). Keeping the phase matching in mind we can express equations (3.23) in the conventional tensor form:

$$\begin{aligned} &P_i^{(1)}(\omega) = \chi_{ij}^{(1)}(\omega)E_j(\omega) \\ &P_i^{(2)}(\omega = \omega_j + \omega_k) = \chi_{ijk}^{(2)}(\omega, \omega_j, \omega_k)E_j(\omega_j)E_k(\omega_k) \\ &P_i^{(3)}(\omega = \omega_j + \omega_k + \omega_l) = \chi_{ijkl}^{(3)}(\omega, \omega_j, \omega_k, \omega_l)E_j(\omega_j)E_k(\omega_k)E_l(\omega_l) \end{aligned} \tag{3.24}$$

An estimation for the ratio of two successive polarization terms of the series eq. (3.22) gives

$$\left|\frac{P^{(n+1)}}{P^{(n)}}\right| = \left|\frac{\chi^{(n+1)}E}{\chi^{(n)}}\right| \tag{3.25}$$

Thus, one usually expects that the lower-order contribution to the nonlinear polarization will be much stronger than the high-order ones. However the tensor $\chi^{(n)}$ is also strongly dependent on the symmetry of the medium. In materials with inversion symmetry, for example one has $\chi^{(2n)}$=0, with n=1,2,3...., and therefore the nonlinear polarization contains only odd-order terms in this case. A medium with inversion symmetry contains a regular lattice of sites such that inversion (the replacing of each atom at coordinate $\vec{r}$, relative to the point, with the one with -$\vec{r}$) leaves the crystal structure unchanged [4]. Let's induce now the even-number higher-order polarization $P^{(2n)}_{\vec{r}} = \chi^{(2n)}E^{(2n)}$ in this medium along the direction $\vec{r}$. Inversion symmetry implies that the polarization $P^{(2n)}_{-\vec{r}} = \chi^{(2n)}E^{(2n)}$ along the $-\vec{r}$ direction should be equal in its absolute value with $P^{(2n)}_{\vec{r}}$ but have an opposite sign. Given the even power of the electric field, this is only possible if $\chi^{(2n)} = 0$. In the non-centrosymetric materials the even order processes are symmetry allowed.

3.1.3 Optical rectification and second harmonic generation

In the following field we will focus on the 2^{nd} order nonlinear polarization induced by an optical excitation. Two electromagnetic plane waves, E_1(t)=A_1(t)cos (ω_1t) and E_2(t)=A_2(t)cos (ω_2t) are incident on a material. $A_{1,2}$(t) are the wave envelopes and $\omega_{1,2}$ are the carrier frequencies. The second order nonlinear polarization $P^{(2)}$ (see eq. (3.24)) can be represented as

$$\begin{aligned} &P^{(2)}(\omega = \omega_1 \pm \omega_2) = \chi^{(2)}_{ijk}(\omega)A_1(t)A_2(t)\cos(\omega_1 t)\cos(\omega_2 t) = \\ &\frac{1}{2}\chi^{(2)}_{ijk}(\omega)A_1(t)A_2(t)(\cos[(\omega_1 - \omega_2)t] + \cos[(\omega_1 + \omega_2)t]) \\ &= P^{(2)}_{\Delta}(\omega) + P^{(2)}_{\Sigma}(\omega) \end{aligned} \tag{3.26}$$

$P^{(2)}(\omega)$ is now a sum of two terms: $P^{(2)}_{\Delta}(\omega)$ containing the difference frequencies and $P^{(2)}_{\Sigma}(\omega)$ containing the sum frequencies. If the two incident electromagnetic waves are identical, i.e. A_1=A_2=A and ω_1 =ω_2 =ω, then the last equation becomes

$$P^{(2)}(2\omega = \omega + \omega) = \frac{1}{2}\chi^{(2)}_{ijk}(2\omega)A^2(t) + \frac{1}{2}\chi^{(2)}_{ijk}(2\omega)A^2(t)\cos(2\omega t) = P^{(2)}_{\Delta}(0) + P^{(2)}_{\Sigma}(2\omega) \tag{3.27}$$

The result consists of two nonzero polarization terms, both dependent on the electric field amplitude. $P^{(2)}_{\Delta}(0)$ is completely independent of the carrier frequency and describes the

effect called *optical rectification*. $P_{\Sigma}^{(2)}(2\omega)$ contains oscillations at the doubled carrier frequency, and describes an effect called *second harmonic generation* (SHG). The carrier-frequency-independent second order polarization term $P_{\Delta}^{(2)}$ is directly proportional with the incident wave intensity. When A(t)=const, i.e. the electromagnetic wave is unmodulated, the optical rectification effect will result in a permanent polarization inside the medium.

In the case of a pulsed electromagnetic wave, the term $P_{\Delta}^{(2)}$ will be time-dependent and according to the wave equation (3.15) will result in electromagnetic radiation with the far-field time-varying electric field strength given by eq. (3.16) with $\mathbf{J} = 0$. In our work we will use this property to generate THz electromagnetic signals in nonlinear optical crystals. One should be aware of the fact that not all nonlinear optical crystals have both good SHG and optical rectification efficiencies. The copropagation of the carrier, second harmonic and optically rectified signals, requires a good phase matching over a very wide frequency range over a considerable optical path inside the crystal, which is not the case for most dielectrics. In general the crystals with a high optical rectification efficiency have very small SHG efficiency and vice versa.

3.1.4 Linear electrooptic effect and phase retardation

When a low-frequency, Ω , or a dc electric field $E_0(\omega \approx 0)$ is applied to a medium, the optical dielectric constant of the medium $\varepsilon(\omega,E_0)$ may depend on the amplitude of the applied field E_0. When the applied field has a small amplitude $\varepsilon(\omega,E_0)$ can be expressed as a power series of E_0 [5]:

$$\varepsilon(\omega, E_0) = \varepsilon^{(1)} + \varepsilon^{(2)}(\omega + \Omega)E_0 + \varepsilon^{(3)}(\omega + 2\Omega)E_0E_0 + ... \tag{3.28}$$

Since D = ε_0 E + P and the polarization can be written as P = $\chi^{(1)}$E + $\chi^{(2)}E^2$ + ..., the nonlinear terms of optical dielectric constant will became

$$\begin{aligned} \varepsilon^{(2)}(\omega + \Omega) &= \frac{1}{\varepsilon_0}\chi^{(2)}(\omega + \Omega) \\ \varepsilon^{(3)}(\omega + 2\Omega) &= \frac{1}{\varepsilon_0}\chi^{(3)}(\omega + 2\Omega) \\ &..... \end{aligned} \tag{3.29}$$

A medium with no inversion symmetry will have an electrooptic effect dominated by the linear term $\varepsilon^{(2)}E_0$. This effect is known as the *linear electrooptic effect* or the *Pockels effect*. The quadratic electric field term $\chi^{(3)}E_0E_0$ will exist in any medium and it is called the *Kerr effect*.

Let's consider the linear electrooptic effect in a crystal. The refractive index ellipsoid describes the spatial dispersion of the crystal refractive index n = $\sqrt{\varepsilon}$ without an applied

electric field.

$$\frac{x^2}{n_x^2} + \frac{y^2}{n_y^2} + \frac{z^2}{n_z^2} = 1, \tag{3.30}$$

x, y, z are the principal dielectric axes, i.e. the axes along which D and P are collinear.

In the presence of an external electric field $E_0(x, y, z)$ the dielectric tensor changes leading to a difference in refractive index. The external field will induce a birefringence in the crystal where the propagating electromagnetic waves polarized along and perpendicularly to the applied field experience an altered refractive index.

Changes in the constants $1/n_x^2, 1/n_y^2, 1/n_z^2$ of the refractive index will reflect the effect of the applied field on the refractive index ellipsoid. Using the same conventions as in [4] the deformed refractive index ellipsoid reads out

$$\left(\frac{1}{n^2}\right)_1 x^2 + \left(\frac{1}{n^2}\right)_2 y^2 + \left(\frac{1}{n^2}\right)_3 z^2 + 2\left(\frac{1}{n^2}\right)_4 yz + 2\left(\frac{1}{n^2}\right)_5 xz + 2\left(\frac{1}{n^2}\right)_6 xy = 1 \tag{3.31}$$

Choosing the axes *x, y, z* parallel to the crystal principal dielectric axes, then without an applied electric field eq. (3.31) will reduce to eq. (3.30) and

$$\left(\frac{1}{n^2}\right)_1\Big|_{E_0=0} = \frac{1}{n_x^2}; \left(\frac{1}{n^2}\right)_2\Big|_{E_0=0} = \frac{1}{n_y^2}; \left(\frac{1}{n^2}\right)_3\Big|_{E_0=0} = \frac{1}{n_z^2} \tag{3.32}$$

and the mixed terms are

$$\left(\frac{1}{n^2}\right)_4\Big|_{E_0=0} = \left(\frac{1}{n^2}\right)_5\Big|_{E_0=0} = \left(\frac{1}{n^2}\right)_6\Big|_{E_0=0} = 0 \tag{3.33}$$

The linear changes in the coefficients $\left(\frac{1}{n^2}\right)_i$, with i= 1...6, induced by the applied electric field $E_0(E_x, E_y, E_z)$ are expressed by

$$\Delta\left(\frac{1}{n^2}\right)_i = \Sigma_{j-1}^3 r_{ij} E_j \tag{3.34}$$

where i runs from 1 to 6, and j from 1 to 3 and denotes the projections of the applied field E_0 on the axes *x,y,z*. The last equation expressed in the matrix form will read:

$$\begin{vmatrix} \Delta\left(\frac{1}{n^2}\right)_1 \\ \Delta\left(\frac{1}{n^2}\right)_2 \\ \Delta\left(\frac{1}{n^2}\right)_3 \\ \Delta\left(\frac{1}{n^2}\right)_4 \\ \Delta\left(\frac{1}{n^2}\right)_5 \\ \Delta\left(\frac{1}{n^2}\right)_6 \end{vmatrix} = \begin{vmatrix} r_{11} & r_{12} & r_{13} \\ r_{21} & r_{22} & r_{23} \\ r_{31} & r_{32} & r_{33} \\ r_{41} & r_{42} & r_{43} \\ r_{51} & r_{52} & r_{53} \\ r_{61} & r_{62} & r_{63} \end{vmatrix} \begin{vmatrix} E_1 \\ E_2 \\ E_3 \end{vmatrix}$$

The tensor r_{ij} is called the electrooptic tensor and strongly depends on the internal symmetry of the material. In centrosymmetric materials, where the second order nonlinear susceptibility $\chi^{(2)} = 0$, all the elements $r_{ij} = 0$.

For the ZnTe crystals used in this work, which have cubic symmetry, $\bar{4}3m$, the electroopic tensor is [4]:

$$\begin{vmatrix} 0 & 0 & 0 \\ 0 & 0 & 0 \\ 0 & 0 & 0 \\ r_{41} & 0 & 0 \\ 0 & r_{41} & 0 \\ 0 & 0 & r_{41} \end{vmatrix}$$

In order to calculate how an electromagnetic wave changes by propagation through an electrooptic material in the presence of an applied electric field, a transformation of the deformed refractive index ellipsoid eq. (3.31) to the principal axes of the original ellipsoid eq. (3.30) is necessary. The deformed refractive index ellipsoid equation will not contain mixed terms. The original indices $n_x, n_y, n_z\ |_{E_0=0}$ will depend on $n_x, n_y, n_z\ |_{E_0}$, E_1, E_2, E_3, and the components of the electrooptic tensor r_{ij}. After this transformation, the principal axes of the deformed index ellipsoid $n_x, n_y, n_z\ |_{E_0}$ in general do not coincide with the principal axes of the original index ellipsoid $n_x, n_y, n_z\ |_{E_0=0}$.

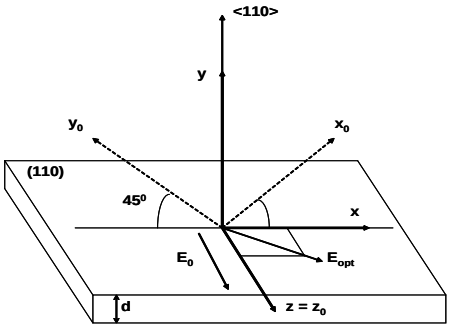

Figure 3.1: Orientation of the principal axes of the original (x_0, y_0, z_0) and the deformed (x,y,z) index ellipsoid due to the linear electrooptic effect in <110> ZnTe crystal. E_0 is applied along $z = z_0$ axis. E_{opt} indicates the polarization plane of an incident plane wave.

In the following we will investigate how the refractive index changes in an <110>

- oriented ZnTe crystal of thickness d. In the absence of an external applied field the refractive indices $n_{x,y,z} = n_0$ are equal in all three directions x_0, y_0 and z_0. If the electric field E_0 is oriented parallel to the z_0 crystal axis, then the deformed index ellipsoid as it follows from (eq. (3.30) and eq. (3.34)) will have the form

$$\frac{x^2}{n_0^2} + \frac{y^2}{n_0^2} + \frac{z^2}{n_0^2} + 2r_{41}E_0xy = 1 \tag{3.35}$$

The applied electric field results in no change of $z = z_0$ axis and in a rotation with 45^0 of the x and y axes around z. The refractive index along the new axes are

$$\begin{aligned} n_x &\approx n_0 + \frac{1}{2}n_0^3 r_{41}E_0 \\ n_y &\approx n_0 - \frac{1}{2}n_0^3 r_{41}E_0 \\ n_z &= n_0 \end{aligned} \tag{3.36}$$

Let us now send a plane electromagnetic wave normal to the crystal surface and polarized at 45^0 with respect to the z axis (its polarization is marked E_{opt} in fig. 3.1). Because the polarization of the electromagnetic wave has 0 projection on the y axis, it will only interact with with the x and z components of the refractive index n_x and n_z, which are different from each other. The incident electromagnetic wave will thus experience a *phase retardation*, because its x and z components will now propagate through the crystal with different velocities. The total phase difference between these two components will be

$$\Delta\phi = \frac{\omega(n_x - n_z)d}{c} = \frac{1}{2}\frac{\omega n_0^3 r_{41}E_0 d}{c} \tag{3.37}$$

where ω is the angular frequency of the incident electromagnetic wave. The phase retardation in nonlinear crystals induced by low-frequency electric fields is one of the most commonly used methods for the detection of the THz transients. This is done by time-resolved sampling of the phase retardation of an ultrashort optical probe laser pulse, induced by the electric field in the incident THz transient.

3.2 Design and characterization of the Terahertz Time-Domain Spectrometer

3.2.1 Generation of picosecond Terahertz pulses

Since the emergence of Terahertz Spectroscopy, in the middle of 80's, there has been a continuous search for new materials with efficient emission of terahertz radiation. A mul-

titude of new materials used for THz generation have been discovered, some of them being able to generate THz radiation with higher bandwidth. As a result, today, a multitude of methods and materials are used for the generation of THz pulses. Between them, the use of photoconductive antenna's based on low-temperature-grown GaAs and Si-GaAs is the oldest method for generating and detecting THz pulses [6–8]. THz radiation can result also from transient conductivity which is based on high-intensity ultrashort laser pulses exciting the surface of an unbiased semiconductor [12]. Synchrotrons and free electron lasers can generate short pulses of far-infrared radiation, typically on the order of 5 -10 ps. It has been shown that laser-generated plasmas can produce radiation up to 4 THz [14, 15]. More recently, there have been notable developments in using a single structure for transmitter and receiver, named transceiver and based on electrooptic crystals [16]. In this case, the electrooptic terahertz transceiver alternately transmits pulsed electromagnetic radiation (optical rectification) and receives the return signal (electrooptic effect) using the same crystal.

Still, probably the most popular choice for THz pulse generation, when working with amplified lasers, is to employ optical rectification in a nonlinear medium. The nonlinear medium is in most of the cases ZnTe but GaAs and GaP have been used as well. It has been shown that organic molecular crystals like DAST [18] and MBANP [19] are also capable of generating THz pulses by optical rectification. They are more efficient than ZnTe crystals of the same thickness, but have not yet found widespread use. In our spectrometer we create THz pulses by optical rectification in a 1 mm thick <110> oriented ZnTe crystal. The generation process is based on an amplified Ti:sapphire laser which provides pulses at 1 KHz repetition rate, with 150 fs pulse duration, and 800 nm wavelength. ZnTe is one of the most popular THz emitters used with near-infrared laser sources since being a wide bandgap semiconductor (E_g(ZnTe) = 2.28 eV) it is basically transparent at the laser pump wavelength, but shows good nonlinear properties. At 800 nm it has both large 2^{nd} order nonlinear susceptibility $\chi^{(2)} = 1.6 \cdot 10^{-7}$ esu [29] and electrooptic coefficient $r_{41} = 4.04\ pm/V$ [20].

The optical rectification process can be understood as the difference frequency analogue of second harmonic generation. In other words, when light interacts with a nonlinear medium and wave mixing between two frequencies, ω_1 and ω_2 occurs, the result is sum-frequency generation, $\omega_1 + \omega_2$, and difference frequency generation, $\omega_1 - \omega_2$ (see eq. (3.26)). In the particular case when $\omega_1 = \omega_2$, one generates both second harmonic and dc pulses. Because the near-IR pulse has a duration of 150 fs, a "dc" pulse corresponding to the envelope of the optical generating pulse rather than a constant dc level.

Alternatively, this generation mechanism can be understood by considering the fact that the optical pulses have significant bandwidths. Thus, the high-frequency components can mix with the low-frequency components within a given pulse to produce a pulse at

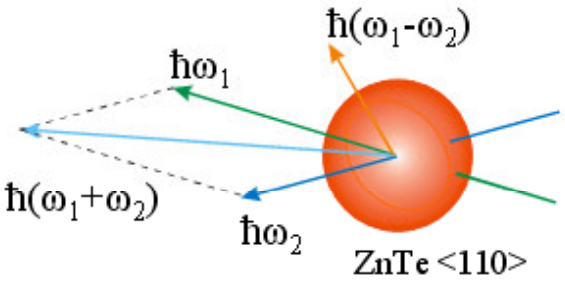

Figure 3.2: Wave mixing between two frequencies ω_1 and ω_2, when light interacts with a nonlinear medium.

the difference frequency. Since the optical pulses have a bandwidth of a few THz, the difference frequencies fall in the THz range. Difference frequency mixing produces a low frequency polarization which follows the envelope of the incident laser pulse. The nonlinear polarization in the time-domain yields:

$$P_i^{(2)}(t) = \chi_{ijk}^{(2)} E_j(t) E_k(t) \tag{3.38}$$

The polarization is directly proportional to the second order nonlinear susceptibility and the intensity of the optical generating pulse. This polarization is not stationary, but moves with the group velocity of the optical pulse. The contribution from the infrared lattice vibration to the low-frequency dielectric response causes the velocity of the source to exceed the radiation velocity. This restricts the bandwidth for efficient phase matching. The phase matching is achieved when the phase of the THz wave travels at the same speed as the optical pulse envelope. After the optical pulse and the THz wave have copropagated through a material of thickness d, the accumulated group velocity mismatch time is

$$\delta(\omega_{THz}) \approx \frac{[n_g(\lambda_{opt}) - n(\omega_{THz})]d}{c} \tag{3.39}$$

assuming a monochromatic THz wave and a delta-function like optical pulse centered at λ_{opt}. $n_g(\lambda_{opt})$ is the optical group index and n(ω_{THz}) the THz phase index. There is a clear trade-off between a broadband response and a long interaction length. Several considerations determine the selection of the material. The material should be transparent to the optical pulse having low absorption and a large electro-optic coefficient. Furthermore,

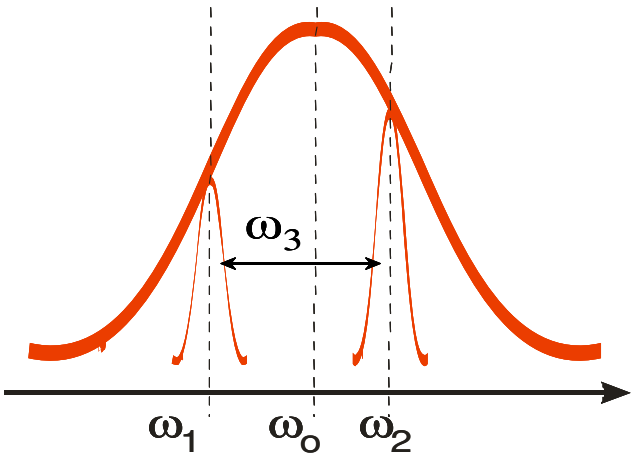

Figure 3.3: The low frequency component of a pulse ω_1, and the high frequency component ω_2, are mixing, producing a pulse at the difference frequency $\omega_3 = \omega_1 - \omega_2$.

the static birefringence in both the optical and the far-infrared regions of the spectrum should be small. ZnTe has a broad TA-phonon absorption line centered at 1.7 THz and one stronger at 3.7 THz in addition to a TO-phonon resonance at 5.3 THz limiting the bandwidth to below 5 THz [21] with a typical crystal thickness of 1 mm.

One advantage of optical rectification is that it is a nonresonant method and the THz pulse width is limited only by the optical laser pulse width (and the phonon-mode absorption of the crystal), and not the response time of the material. Some of the shortest THz pulses to date, with bandwidths up to 100 THz and beyond have been generated in this or a similar fashion [22, 24, 27]. Kubler *et. al.* have used a 20 μm thick GaSe crystal to generate THz pulses with a bandwidth beyond 120 THz [22]. In a THz spectrometer, the generated radiation bandwidth can be tuned between 2.5 THz and 100 THz, by choice of the appropriate nonlinear medium and optical generating pulse length.

Let us finally address the issue of the energy flow in the THz generation process using optically transparent nonlinear crystals. In the THz generation approaches utilizing the real optical excitation of the free carriers, for instance in the photoconductive THz generation (see for example [28]), the energy of the THz pulse is drawn from the external electrical circuit. But in our case no external circuit exists, and the laser pulse is not absorbed by the emitter crystal, since the crystal is transparent to the laser pulse wavelength. The generation crystal also does not cool down as a result of THz generation process. Therefore the only energy source for the emitted THz pulse is the laser pulse

itself. Shimizu and Yamanishi [30] have theoretically shown that the THz pulse emitted by optical rectification in a transparent nonlinear crystal draws its energy from the generation laser pulse due to the redshift of the wavelength of the photons in this laser pulse, whereas the number of incident photons is always conserved, since no real absorption is taking place. It should be mentioned here that the value of this redshift should be very small, given the huge energy stored in the laser pulse and quite a moderate energy emitted with the THz pulse. To the best of our knowledge no experimental demonstration of such redshift has been done so far.

3.2.2 Detection of Terahertz pulses

Once the THz pulses have been generated, the need for a reliable detection scheme becomes a must. In the THz spectroscopy development period a multitude of detection methods have been constructed. The oldest one is the photoconductive antenna [6–8], based on low-temperature-grown GaAs and Si-GaAs. When a high-power low-repetition-rate experiment or a destructive experiment is performed, a single-shot detection is desirable (it is possible to collect an entire THz waveform without having to scan a delay line) [33–36]. Nahata and Heinz have demonstrated that it is possible to detect THz pulses via optical second harmonic generation [37]. Polarization modulation, as opposed to amplitude modulation, when using optoelectronic detection has also been demonstrated [38].

Although many THz detection methods exist, the photoconductive antennas and free space electrooptic sampling remain the workhorses of THz detection. In our setup we are detecting THz pulses via free space electrooptic sampling (FSEOS). The reason is that when using an amplified laser system (Ti:Sapphire in our case), the pulses are detected best via free space electrooptic sampling rather than photoconductive dipole antennas (PDA's) [24, 39]. It has the advantage that it is a nonresonant method of detection, so the potential for damaging the detector crystal with the focused readout beam is much lower. The FSEOS is based on the electric field of a THz pulse inducing a small birefringence in an electro-optic crystal through a non-linearity of the first order (Pockels effect). Passing through such crystal, the initially linearly polarized optical probe beam gains a small elliptical polarization. To a first approximation, this ellipticity is proportional to the electric field applied to the crystal, i.e. to the THz pulse in every certain moment of time. Because the THz field is much longer than the optical probe pulse (several ps versus ~150 fs), the THz electric field as experienced by the sampling pulse can be approximated as a dc bias field. Therefore, varying the delay between the THz and optical probe pulse, the whole time profile of the first can be traced. As an FSEOS active medium, a variety of dielectric materials like $LiTaO_3$ [40, 45] and ZnTe [45] or polymers

polarized by externally applied field [40, 41] is employed.

Passing through the electro-optic crystal, the y' and z' components of the electric field of the incident optical wave acquire the phase shift:

$$\delta\phi = \frac{\omega}{c} n^3 r_{231} E_{y'} dx' \tag{3.40}$$

with $r_{231} = 4{\cdot}10^{-12}$ m/V for ZnTe. In the absence of the THz field (E_{THz}=0), the phase shift is zero and the polarization of the probe stays linear. When the THz pulse is present, the phase shift leads to a slightly elliptical polarization (see fig. 3.2).

In practice, a quarter-wave plate is placed behind the electro-optic crystal to make the initially linear polarization of the probe beam (at $E_{THz} = 0$) circular. A Wollatson prism separates its y'' and z'' components and sends them to a differential detector which is connected to a preamplifier and a lock-in amplifier. With no THz present, the components have equal intensity and the differential signal is zero. When the THz field is applied, a nonzero phase difference of the two components appears. According to eq. (3.40), the phase difference is proportional not only to the magnitude of the applied field but also to its sign which makes the whole detection method phase-sensitive.

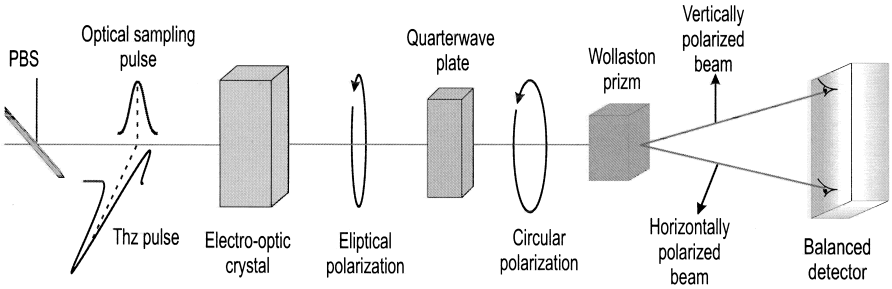

Figure 3.4: Schematics of free space electrooptic sampling detection. PBS - pellicle beam splitter.

We use the FSEOS geometry with the THz and probe beams propagating collinearly through the sensor crystal. For this purpose we use a 1" beam splitter made of very thin polymer transparent for THz radiation and reflecting around 5 percent of optical radiation (so-called pellicle beamsplitter, or PBS). The major advantage of a PBS is that thanks to its thickness, does not lower the temporal resolution of the system through multiple internal reflections. The disadvantage is that is extremely fragile and sensitive to even small vibrations of the air in the laboratory. The highest signal to noise ratio (SNR) reached in our spectrometer with FSEOS is 1000:1. Compared to photoconducting antenna detectors , the FSEOS is somewhat less sensitive but is free from artifacts typical for PDA

like a broad minimum before the main peak and the drifting background. It is also much more mechanically stable than PDA and does not require very precise optical adjustment.

3.3 Transmission Time-Domain Terahertz Spectrometer

Our THz spectrometer is driven by a commercial femtosecond Ti:Sapphire (Ti:Sa) amplifier (Hurricane, Spectra Physics). A schematic representation of this laser system is depicted in fig. 3.5.

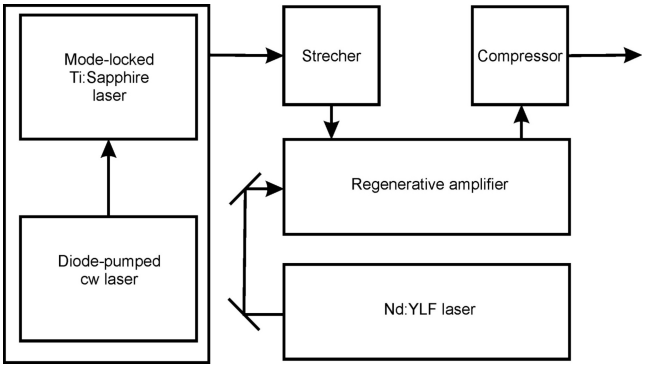

Figure 3.5: Typical amplified femtosecond laser system. An cw diode-pumped laser pumps a mode-locked Ti:Sapphire oscillator, which produces approximately 800 mW of 150 fs and 800 nm pulses. These pulses are directed to the stretcher to be stretched, amplified and then recompressed. The regenerative amplifier is pumped with a Nd:YLF laser.

It is composed from five main components: a seeding laser (Mai-Tai), a pump laser, a stretcher, a compressor and a regenerative amplifier. The Mai-Tai consists of two lasers, a continuous-wave (cw) diode-pumped laser (Millenia) and a mode locked Ti:Sapphire resonator, as well as a power supply unit, chiller and other necessary elements. The cw diode-pumped laser emission is 532 nm at an average output power of 5 W. Because the Ti:Sapphire has a broad absorption band in the green and blue region, the 532 nm cw-laser output acts as an ideal pump for the Ti:Sapphire cavity. A second part of Mai-Tai is a mode-locked Ti:Sapphire cavity which consists of Ti:Sapphire rod, focusing mirrors and other optics. The Mai-Tai is thus able to deliver continuously tunable pulsed power output at 80 MHz repetition rate over a range of near infrared wavelengths from 790 to 810 nm with a pulse duration of about 90 fs. The Evolution laser is a diode-pumped, intracavity doubled Nd:YLF laser able to produce Q-switched pulses with an

average power of 6 W at 523.5 nm at a repetition rate of 1 kHz. The main elements of the Evolution laser are a diode-pumped Nd:YLF laser, an optical resonator, an acousto-optical Q-switch and a lithium triborate (LBO) frequency doubling crystal. The lasing material (Nd:YLF) has two laser transitions at 1053 nm and 1047 nm with different polarizations. The Evolution system is using the 1047 nm line, due to a higher gain cross section. Q-switching is achieved by diffracting the light beam on an optical phase grating which is generated by launching an ultrasonic wave on a transparent material. The laser can be brought into the higher Q-state by controlling the voltage supply to the piezo-electric transducer which drives the ultrasonic wave.

The ultra short pulses have a very high saturation fluorescence which can lead to self focusing. In order to avoid damage to the optics inside the amplifier cavity, the seed pulses are therefore stretched before entering the amplifier cavity. When a pulse is stretched its peak power is distributed over a relatively large time span and hence its power density is lowered. The pulse stretching is based on dispersion by diffraction gratings. Thus the Hurricane Ti:Sapphire regenerative amplifier is designed to amplify individual pulses from a mode-locked Ti:Sapphire laser. Typically, an input pulse of energy of only a few nanojoules can be amplified to over 1 mJ. The output pulse of the Hurricane has an energy of 750 μJ and a width of 150 fs operating at 1 kHz. In pump-probe experiments this low repetition rate allows the sample to relax completely before the next pulse arrives, thus minimizing the heating effect due to the pile-up of pulses.

In the following we will describe the THz time-domain spectrometer based on optical rectification of the 150 fs pulses with the central wavelength of approximately 800 nm in a ZnTe crystal and detection of the THz pulses in another ZnTe crystal using free-space electrooptic sampling (FSEOS) technique (see fig. 3.6). The emitter crystal is <110>-oriented and 1 mm thick. Detection is realized using a <110>-oriented ZnTe crystal of 0.2 mm mounted on a <100>-oriented ZnTe crystal of 0.5 mm. When a short microwave pulse is applied on the detection crystal, the group-velocity mismatching of ZnTe must be considered. The measured group-velocity mismatching of ZnTe is 0.4 ps/mm. In order to reduce walk-off for better temporal resolution, the thinner <110> crystal provides shorter convolution window (about 0.1 ps), and the thicker <100> crystal delays the reflected THz pulse, with no contribution to the electrooptic phase retardation. The disadvantage of using a thinner crystal is the reduction of electrooptic signal, due to the shorter interaction length [45]. ZnTe is one of the most popular choices for THz emitters and detectors because having a wide bandgap ($E_g(ZnTe) = 2.28\ eV$), it is basically transparent at the laser pulse wavelength, but shows good nonlinear properties. For 800 nm pulses it has large 2^{nd} order nonlinear susceptibility $\chi^{(2)} = 1.6 \cdot 10^{-7}$ esu [29] and large electrooptic coefficient $r_{41} = 4.04$ pm/V [20]. The 150 fs laser pulse with the central wavelength around 800 nm excites a transient nonlinear polarization spike in the emit-

ter ZnTe crystal, which produces an electromagnetic pulse with the frequency spectrum in the THz range. This process is described in sections 2.1.1 and 2.1.3 by the equations (3.15), (3.16), (3.27). The THz pulse is guided to the detector ZnTe crystal by the off-axis parabolic mirrors. In the last part of my studies, our THz lab had to be moved to another

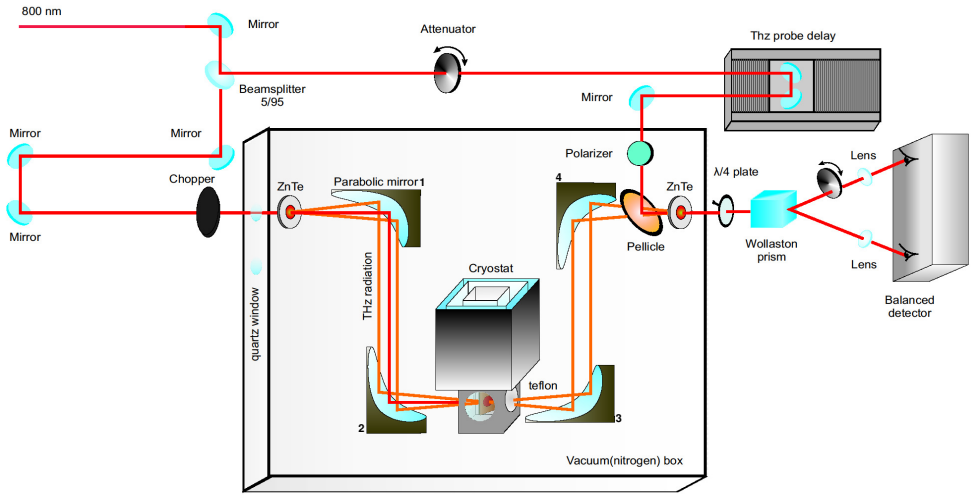

Figure 3.6: Schematic representation of the terahertz time-domain transmission spectrometer. Please be aware that parabolic mirrors 1 and 3 are not well oriented.

building. In the reconstruction process, parabolic mirrors 1 and 3 (see fig. 3.6) were wrongly oriented. Therefore, the THz beam trajectory is not passing any more through the center of the parabolas, which means that it is not reflected under a 90 degrees angle, without abberations. Because of that, THz beam will suffer from optical aberration, more precisely the focus will be bigger and will form at a different point with respect to the focus formed in a correct paraboloid orientation. The cryostat was positioned for a maximum gain in signal, which is in the focus of the THz beam. Another consequence will be a THz wave front tilt which was estimated to a maximum of 2 ps, for one single not well oriented paraboloid.

Once the THz pulse is transmitted to the surface of the detector ZnTe crystal, its

electric field induces a birefringence in this crystal. This birefringence is detected by the phase retardation (see eq. (3.37)) of the very weak (less than 3 percent of the Hurricane output power) 800 nm laser probe pulse which has a prealigned polarization. This probe laser pulse is temporally delayed with respect to the pump laser used for THz generation using the variable delay line. It is therefore possible to measure the phase retardation (which is proportional to the electric field of the THz pulse) with a time resolution of about 150 fs. Considering that both THz pump and THz probe laser pulses originate from the same laser beam and normally have the same duration, we can state the fundamental limitation of the THz-TDS method: it is not possible to measure THz signals which are shorter than the probe laser pulse itself. Therefore in a conventional THz-TDS setup the bandwidth of the THz pulse cannot exceed that of the detection probe pulse. After the propagation through the quarterwave plate, the phase-retarded optical probe pulse will become elliptically polarized, which will result in different light intensities incident on the two photodiodes of the differential detector. The difference in voltages detected by these photodiodes will be proportional to the induced phase retardation, and therefore (see eq. (3.37)) to the electric field strength in the THz pulse. Varying the delay between the THz pulse and the optical probe one can therefore temporally sample the electric field in the THz pulse. Taking into account eq. (3.37), the measured electric field in the THz pulse in the case of the FSEOS in cubic electrooptic crystals can be estimated as

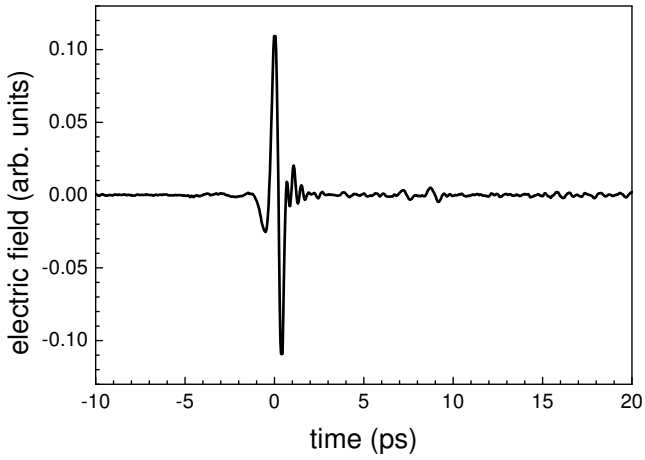

Figure 3.7: Time trace of a typical terahertz pulse obtained with our THz spectrometer.

$$E_{THz} = \frac{2\Delta V}{V_{max}} \cdot \frac{c}{\omega n_0^3 r_{41} d}, \tag{3.41}$$

where ΔV is the difference in the voltages detected by the two photodiodes of the differential detector. V_{max} is the voltage produced by each of the photodiodes when they are illuminated with the probe beam, when no THz field is applied. Then $\Delta V = V_{max} - V_{max} = 0$. n_0 and r_{41} are the refractive index and the electrooptic coefficient of the nonlinear crystal at the frequency of the probe beam ω. d is the thickness of the crystal. The electrooptic signal ΔV in our experiment was first preamplified and then read by a commercial lock-in amplifier SR 830 DSP at a frequency of 166.6 Hz corresponding to 1/6 of the Ti:Sapphire amplifier repetition rate. The THz generation beam was modulated at this frequency with a chopper (see fig. 3.19). For the ZnTe crystal probed at 800 nm $n_0 = 3.22$ [43]. In the case of 1 mm thickness, the electric field in the THz pulse is approximately

$$E_{THz} = \frac{\Delta V}{V_{max}} \cdot 2.67 \cdot 10^4 [V/cm], \tag{3.42}$$

THz generation by optical rectification of ultrashort laser pulses was first demonstrated

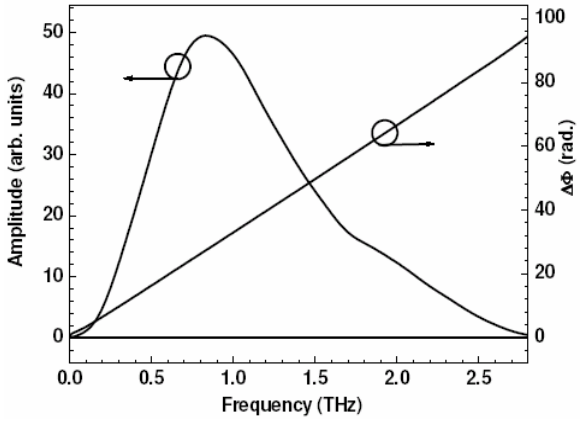

Figure 3.8: Amplitude and phase of the terahertz time trace Fourier transform.

by the group of Y. R. Shen in 1971 [44]. The FSEOS detection scheme was first introduced by the groups of X. C. Zhang [45] and P. Uhd Jepsen and H. Helm [28] in 1996. Both these techniques have been widely used ever since and allow for coherent detection of the electric field temporal evolution in ultrashort transients. Recently the generation and detection of THz pulses with the peak electric field strength of the order of 1 MV/cm was demonstrated using optical rectification and FSEOS detection schemes [24]. A typical time trace of a THz pulse generated and detected in our THz spectrometer is shown

in fig. 3.7, while its amplitude and phase frequency dependent spectra are shown in fig. 3.8. This pulse was generated by the 800 nm central wavelength , 150 fs long laser pulse with the fluence of approximately 0.5 mJ/cm^2.

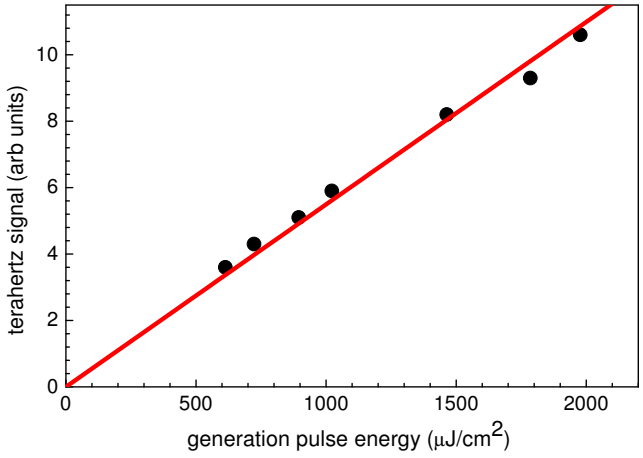

Figure 3.9: Input laser-power dependence of the terahertz pulse fluence for <110> ZnTe.

The THz pulse has a relatively complicated shape with a main single-cycle oscillation, followed by decaying anharmonic oscillations. The maximum signal-to-noise (S/N) ratio of this pulse is about 10^3. This THz pulse has a useful bandwidth in the range 0.2 - 2.5 THz, which is considerably smaller than the bandwidth of the 150 fs excitation laser pulse. The temporal shape and bandwidth of a THz pulse produced by optical rectification in an optically transparent nonlinear crystal is determined by the temporal shape and bandwidth of the excitation pulse as well as by the phase mismatch between the optical and THz pulses copropagating through the crystal and the THz absorption by phonons in the crystal. Fig. 3.10 displays the terahertz pulse parameters.

The THz center, width and amplitude are clearly defined. Another two definition will be also useful: we will call a positive part of the THz peak, the peak which is situated above $y = 0$ axis, and a negative part of the THz peak the peak which is situated below $y = 0$ axis.

By varying the excitation (pump) power, it is possible to obtain a power dependence of the terahertz emission from the <110> oriented and 1 mm thick ZnTe generation crystal. Fig. 3.9 shows the measured input power dependence of the terahertz signal. The terahertz pulse fluence grows linearly with the energy carried in the generating pulse. However at power densities above 3 mJ/cm^2 white light generation effects start to occur in ZnTe as well as optical damage to the crystal [25].

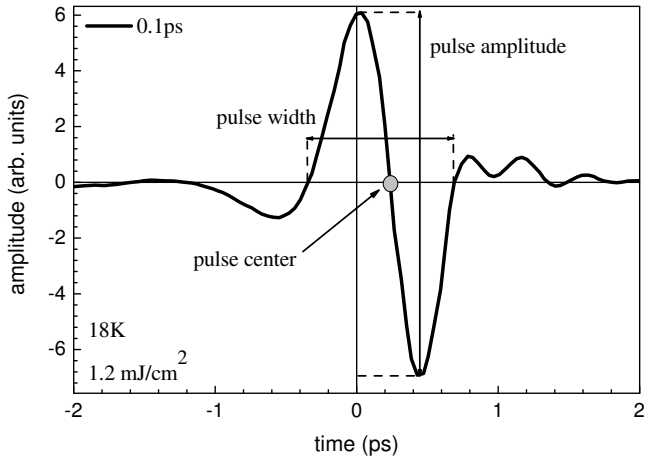

Figure 3.10: Terahertz pulse in the time-domain, transmitted through a Cu_2O sample at 18 K, after 0.1 ps from the optical excitation. The sample is excited with 1.2 mJ/cm^2. The pulse center, width and amplitude are defined. The THz pulse peak which is situated above $y = 0$ axis will be defined as positive peak, while the THz peak situated below $y = 0$ axis will be defined as negative peak.

In order to determine the terahertz beam focus we performed pulse measurements when the pulse was propagating through a pinhole with different diameters. Figure 3.11 displays the terahertz pulses, as well as their fourier transforms, after propagating through the pinhole with the diameter of 2, 3, 4 and 5 mm. A decrease in terahertz electric field amplitude with the pinhole diameter can be seen. This electric field pulse amplitude decrease results in a decrease of spectral weight in the Fourier spectra of these pulses. Considering the pulse intensity variation, we determine the terahertz beam focus to be in the order of 3.5 mm.

The central part of the terahertz spectrometer is concealed in an aluminium home - made box (see fig. 3.19). To be more precise, the entire terahertz beam trajectory between the generation crystal and the detection crystal is situated inside this box. This is to prevent complications due to water vapor which is always present in air has a very pronounced signature in the range of our THz spectrometer (from 0.2 until 2.5 THz). In order to create a water vapor free environment along the THz beam path two approaches can be followed. The first approach, and the most spread among experimentalists, would be to purge the box with pure N_2 gas. The second approach, not so often used at the moment, is to create relatively modest vacuum conditions inside the box (10^{-3} mbar),

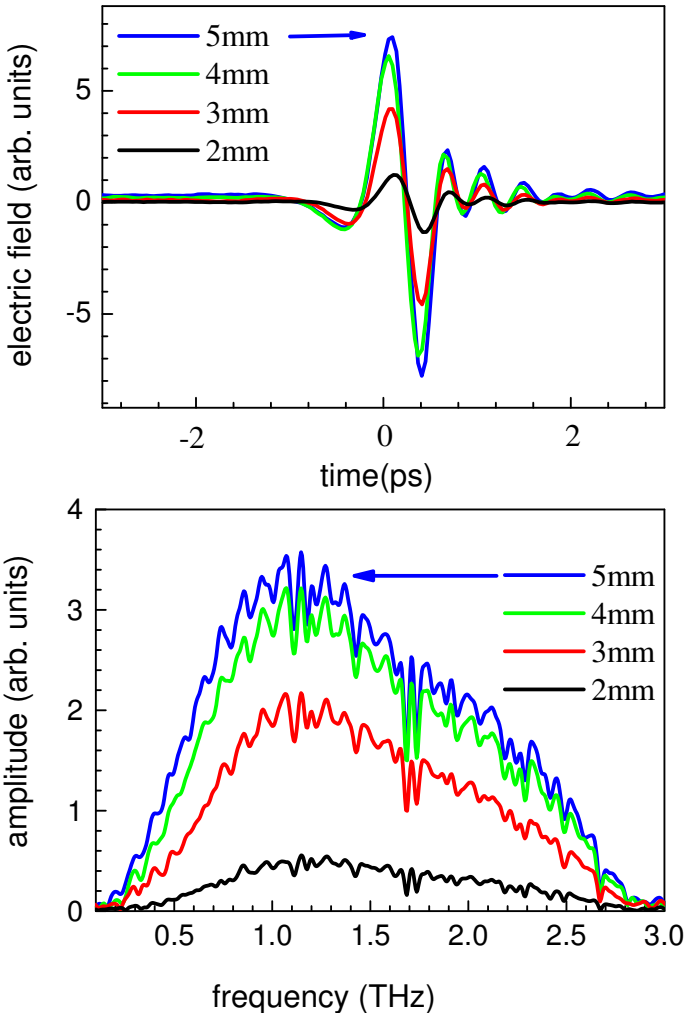

Figure 3.11: Terahertz pulse measured after propagating through a pinhole with different diameters and their Fourier transforms.

which should eliminate also almost completely the water vapor. In the following we will do a comparison between these two possibilities and will show that in our opinion, a vacuum environment is more suitable for terahertz experiments than a N_2 environment. All frequency spectra presented in the next figure are characteristics of the system used to generate the radiation and any media through which the radiation has propagated. Ter-

ahertz transients of approximately 45 ps length have been measured in three different box atmospheres: air, pure N_2 gas and vacuum. Their Fourier transforms are depicted

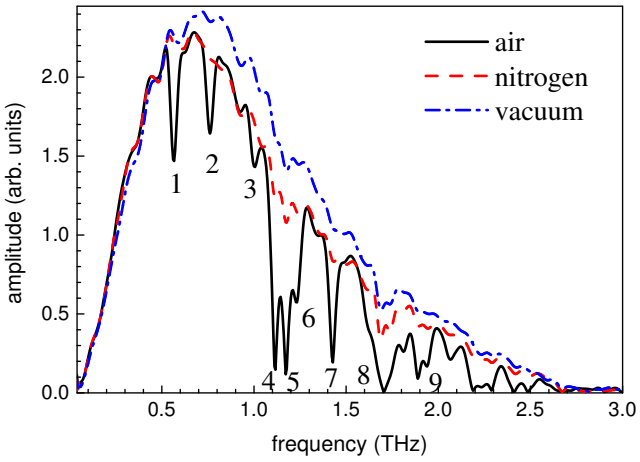

Figure 3.12: Terahertz spectra of three different propagation media: air (continuous line), N_2 gas (dashed line) and vacuum (dash dot line).

in fig. 3.12. While in the air spectrum, nine clear absorption lines are present, in the N_2 spectrum only lines 5 and 8 are visible and in the vacuum spectrum only line 8 can be distinguished. comparing the spectra we attribute the nine absorption lines as follows: lines 1, 2, 3, 4, 5, 6, 7, 9 could be attributed to the presence of water vapor [26], while line 8 can be attributed partly to the ZnTe generation crystal and partly to water vapor, since in vacuum spectra some absorption remains. The spectrum measured in air has the lowest spectral intensity due to the strong water vapor absorption. In the N_2 spectrum besides the ZnTe absorption line which cannot be suppressed, one can still distinguish a very weak water absorption line (line 5). The vacuum spectra contain the same lines as in N_2, but the spectral intensity is the largest between the three displayed spectra. Looking at the terahertz transients, the best signal to noise ratio was obtained from the transient measured in vacuum. Because the vacuum spectra showed the largest spectral intensity and the best signal to noise ratio, we conclude that the best media for the terahertz measurements is vacuum.

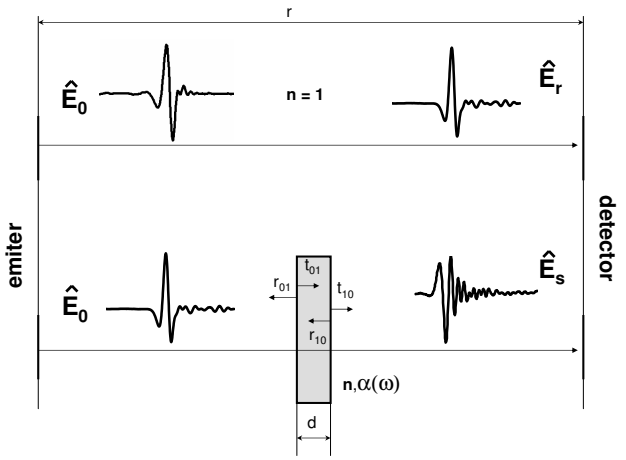

Figure 3.13: $\hat{E}_r$ and $\hat{E}_s$ are the THz signals transmitted through free space (reference pulse) and through the free space and sample. r is the length of the optical path between emitter and detector and d is the sample thickness. r_{01},t_{01} and r_{10},t_{10} are the amplitude reflection and transmission coefficients at the front, and respectively the back of the sample. n(ω) and $\alpha(\omega)$ are the frequency dependent refractive index and power absorption coefficient of the sample.

3.3.1 Propagation of an electromagnetic wave packet through the medium. Terahertz spectral analysis.

In the following we will concentrate over the propagation of a linearly polarized electromagnetic signal through a plan-parallel slab of dispersive medium, i.e. a medium with frequency-dependent refractive index and absorption coefficient. Fig. 3.13 is a schematic representation of the propagation of a THz pulse through the sample with frequency-dependent refractive index n(ω) and power absorption coefficient $\alpha(\omega)$. The free-space signal $\hat{E}_r$ only changes due to the optical components encountered during propagation. We call these changes the system response. The sample signal $\hat{E}_s$ however does experience, besides the system response, reflection losses at the sample's interfaces as well as absorption inside the sample. The extraction of the dielectric properties of the sample, such as refractive index and power absorption coefficient is most easily performed in the frequency-domain, which is done using Fourier transformation. In the following

equations all parameters are frequency-dependent. The detected THz signals propagated through the free-space $\hat{E}_r$ and through both free-space and sample $\hat{E}_s$ have a complex form

$$\begin{aligned}\hat{E}_r &= E_0 e^{ikr} = E_0 e^{i\phi_{free}} \\ \hat{E}_s &= E_0 t_{01} t_{10} e^{ik(r-d)} e^{i\hat{n}kd} = E_s e^{i\phi_{sample}}\end{aligned} \tag{3.43}$$

In this equations E_0 is the electric field strength of the reference pulse, $k = \omega/c$ is the free-space wavevector, r is the length of the optical path, d is the sample thickness, $\hat{n} = n + i\kappa$ is the sample complex refractive index, and t_{01} and t_{10} are the amplitude transmission coefficients at the front and back surfaces of the sample. The electric fields $\hat{E}_s$ and $\hat{E}_r$ in complex form are defined by their amplitude and phases E_s, ϕ_{sample} and E_0, ϕ_{free}.

The amplitude reflection and transmission coefficients at the front and back surfaces of the sample in the case of normal incidence are

$$\begin{aligned}r_{01} &= \frac{1-\hat{n}}{1+\hat{n}}; t_{01} = 1 - r_{01} \\ r_{10} &= \frac{\hat{n}-1}{1+\hat{n}}; t_{10} = 1 - r_{10}\end{aligned} \tag{3.44}$$

Knowing that the power absorption coefficient $\alpha = 2k\kappa$ and taking into account eqs. (3.44) we can write the ratio of the electric fields $\hat{E}_r$ and $\hat{E}_s$ as

$$\frac{\hat{E}_s}{\hat{E}_r} = \frac{4\hat{n}}{(1+\hat{n})^2} e^{-\frac{\alpha}{2}d} e^{i(n-1)kd} = \frac{E_s}{E_0} e^{i(\phi_{sample}-\phi_{free})} \tag{3.45}$$

Performing a complex fit of the experimentally obtained transmission with the theoretical one displayed in eq. (3.45), the real and imaginary refractive index, n and κ are obtained.

The real refractive index and the absorption coefficient, α, can also be obtained considering the following approximation: neglecting the losses suffered due to absorption at the air - sample interfaces (i.e. taking $\kappa = 0$ in the first term of eq. (3.45), $4\hat{n}/(1+\hat{n})^2$). This approximation is valid in the case of relatively low-absorbing samples of any thickness, or optically thick but relatively high-absorbing samples. In this case, the refractive index in eq. (3.44) will became real (the absorptive component κ is neglected) and the transmission becomes

$$\frac{\hat{E}_s}{\hat{E}_r} = \frac{4n}{(1+n)^2} e^{-\frac{\alpha}{2}d} e^{i(n-1)kd} = \frac{E_s}{E_0} e^{i(\phi_{sample}-\phi_{free})} \tag{3.46}$$

Therefore from the measured phase difference of the sample and reference pulses, and taking into account that $\omega = 2\pi f$, f being the frequency, one can obtain the frequency dependent real part of the refractive index

$$n = \frac{(\phi_{sample} - \phi_{free})}{\frac{2\pi f}{c} d} + 1 \tag{3.47}$$

Having calculated the refractive index one can separate the reflection and absorption losses in the sample. The power absorption coefficient of the sample will be then

$$\alpha = -\frac{2}{d} \ln \left[\frac{E_s}{E_0} \frac{(1+n)^2}{4n} \right] \tag{3.48}$$

All the results presented in this work have been obtained using a procedure which does not employ the last mentioned approximation (neglecting the absorption losses at the sample - air interfaces). We have chosen to perform the fit of the experimentally obtained transmission with the theoretical transmission.

In the following we present the results of THz-TDS on a 0.73 mm thick Cu_2O crystal at room temperature, using a 1 mm thick <110> - oriented ZnTe crystals for emission and a double ZnTe crystal: a 0.2 mm <110> oriented crystal glued on a 0.5 mm <100> for detection. Fig. 3.14 shows the reference (free space) and the sample THz transients

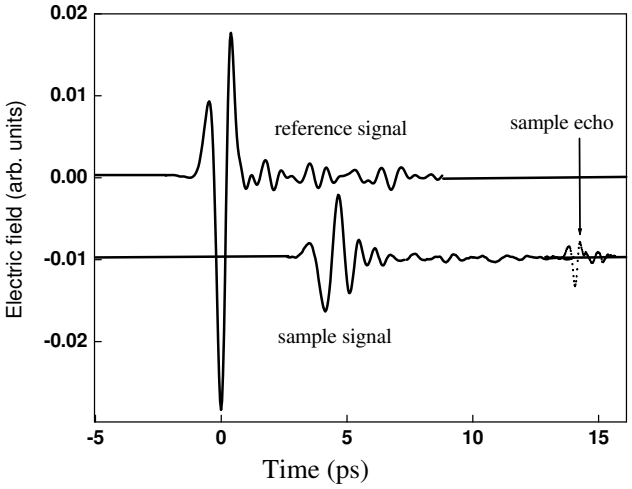

Figure 3.14: THz-TDS on a 0.73 mm thick Cu_2O crystal at room temperature. Measured THz time-domain signals: raw reference signal (upper solid line), raw sample signal (lower line) and sample with removed emitter echo (lower dotted line). The time-domain signals were vertically separated for clarity. time t = 0 is set to be the time where the main peak of the THz pulse is located.

are shown.

The sample THz pulsewas offset from zero for clarity. The time t = 0 has been chosen to be the time where the main peak of the THz pulse is placed. In the beginning and the end, both pulses have been set to zero. One can notice that the main feature of the sample

signal appears approximately 4 ps later than the main feature of the reference pulse, so one could immediately estimate $n_{Cu_2O}(THz)$ using the simple relation $\Delta t = (n-1)d/c$ (where d is the sample thickness and c is the speed of light in vacuum) to find $n \approx 2.7$. This sample pulse delay results from the propagation through the sample, whose refractive index is greater than 1. It has smaller amplitude and its shape is distorted in comparison to the reference pulse. This results from the frequency dependent absorption coefficient and refractive index of the Cu_2O sample crystal. In the sample signal, a main

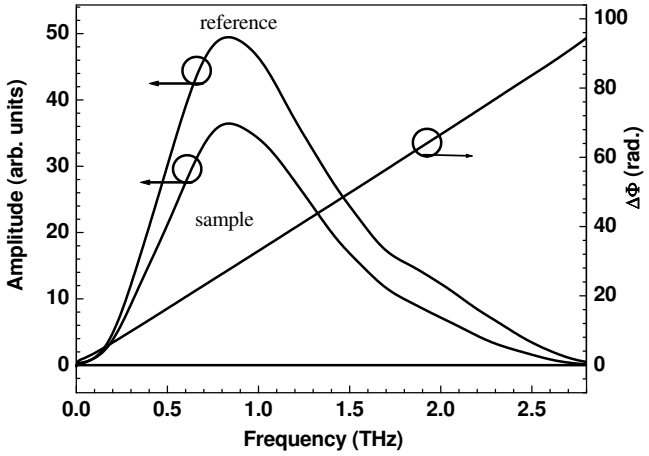

Figure 3.15: Frequency domain amplitude reference and sample (with the echo parts removed) and the phase difference between them.

THz peak appears at 4 ps followed by another feature at 10 ps distance. This feature originates from the etalon reflection in the plan parallel sample, i.e. it is a part of the main THz signal after it made a round trip in the sample. Knowing the sample refractive index we have calculated that in order to travel two sample lengths, the THz reflected pulse will need approximately 9.82 ps. The etalon reflection might be suppressed or removed by using a wedged sample. This echo signal has a distorted time shape and is much weaker than the main pulse. Nevertheless, if Fourier transform of the THz transient and the echo is performed, the echo will influence the transform, leading to an incorrect spectrum. In order to avoid this inconvenience, one can pad the echo part of the time-domain THz signal with zeroes, since the oscillations from the main pulse are already strongly damped at this point. The time-domain THz signal with a zero-padded echo part is shown by the solid line in the figure.

Fig. 3.15 presents the amplitude spectra of the reference and sample THz pulses as well as the phase difference induced by the propagation through the sample in the frequency domain. The amplitude spectra have their maxima at around 1 THz. The reference and sample amplitude spectra have a cut-off frequency of approximately 2.3 THz. As discussed before, the limitation of the reference spectrum is related to the process of generation and detection in ZnTe crystals. The noise floor is approximately 0.0025, which makes the maximum amplitude dynamic range (DR) of about 400 for the reference and the sample spectra.

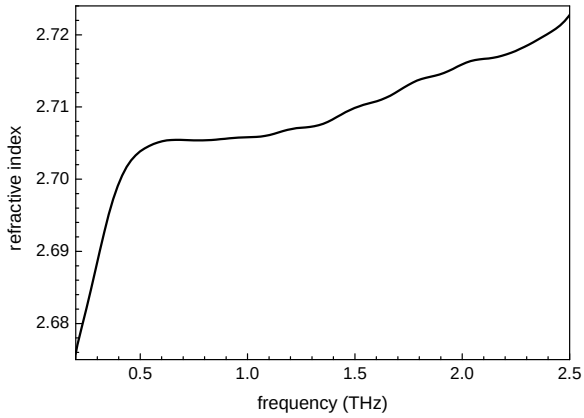

Figure 3.16: Frequency dependent refractive index of the Cu_2O crystal at 17 K calculated from the amplitude and phase spectra.

In fig. 3.16 and fig. 3.17 the refractive index and absorption spectra, respectively, of the Cu_2O crystal at room temperature are shown. These refractive index and absorption spectra are calculated from the amplitude and phase spectra shown in fig. 4.10 using the formulas eq. (3.47) and eq. (3.48). The spectra contain useful information in the range 0.2-2.5 THz. A definition of the spectral limits of reliability for the obtained information can be obtained taking into account the frequency-dependent dynamic range (DR) of the amplitude spectra. As was shown by Jepsen and Fischer [31], one can define the frequency-dependent dynamic range of the measured absorption spectrum based on the signal-to-noise consideration. The maximal frequency-dependent absorption coefficient that can be reliably measured with THz-TDS follows from eq. (3.48) and is calculated

using the formula:

$$\alpha_{max} = \frac{2}{d} \ln \left[DR \frac{4n}{(1+n)^2} \right] \tag{3.49}$$

where d is the sample thickness, DR is the frequency-dependent dynamic range, and n is the frequency-dependent refractive index.

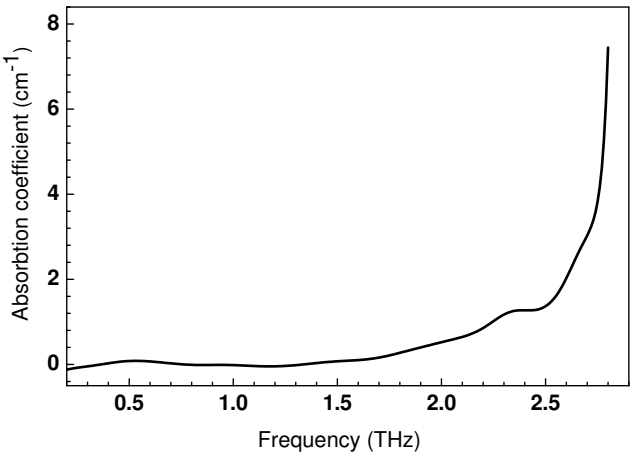

Figure 3.17: Power absorption coefficient of the Cu_2O crystal at 17 K calculated from the amplitude and phase spectra.

The frequency resolution of the THz-TDS is given by the time step and the number of data points in the time-domain measurement $\Delta f = \frac{1}{N}\frac{1}{dt}$, where N is the number of data points in the THz time-domain signal and dt is the time step. The fast digital Fourier transform method (FFT) is used to perform the Fourier transforms numerically. Its performance is best when the number of data points N is a power of 2. Using the high calculus power of the modern computers, performing a FFT transform becomes an easy task. In the measurements presented above the raw data consists of 625 data points with a time step of 40 fs, thus making the whole time scan of 25 ps. In order to reach the nearest power of 2 value which is 1024, the time-domain signals were padded with zeroes after the last measured data point. The reference signal was padded with zeroes already after the 532 - th data point in order to avoid the Fabry-Perot effects in the frequency domain caused by the echo of the sample (see fig. 3.14). This operation did not affected the integrity of the measured and calculated data, because in this range there was already no signal above the noise related to the main THz oscillation. Thus, the frequency resolution of our experiment was $\Delta f = \frac{1}{625} \cdot \frac{1}{0.04} = 0.04$ THz. It should be mentioned that the zero padding and removal of the echoes in the time-domain data should be performed

very carefully because if the meaningful part of the original signal is cut, the frequency domain data will contain false features and lack the true ones.

3.4 Time-Resolved Optical-Pump Terahertz-Probe Spectroscopy

Time resolved measurements are very important in condensed matter systems because they can resolve dynamical processes at fundamental time scales of the electronic and nuclear motion. In a typical time-resolved optical pump-probe experiment, a short laser pulse is split into an intense pump pulse and a weaker probe pulse. The pump pulse induces a change in the sample and the probe pulse measures the induced change in the sample. Varying the delay between the pump pulse and the probe pulse one can monitor the temporal development of the induced change. This development, which we measure in transmission ΔT/T, contains information about the relaxation dynamics of the sample. Measurements of the dynamics of hot-electron relaxation in semiconductors give important information about the physics of nonequilibrium phenomena in these materials as well as information about the carrier-carrier and carrier-phonon interaction, which are of fundamental interest in semiconductor physics.

The transiently induced change in transmission ΔT/T, in the case of small perturbations is connected to the induced changes in the dielectric function, $\varepsilon = \varepsilon_1 + i\varepsilon_2$, of the sample through

$$\Delta T = \frac{\partial lnT}{\partial \varepsilon_1}\Delta\varepsilon_1 + \frac{\partial lnT}{\partial \varepsilon_2}\Delta\varepsilon_2 \tag{3.50}$$

which contains the electronic properties of the material. Here $\Delta\varepsilon_1(\Delta\varepsilon_2)$ represents the induced change in the real (imaginary) part of $\tilde{\varepsilon}$.

However, a potential disadvantage of regular optical pump-probe experiments is that the probe energy, typically 1.5 eV or higher, is much larger than the relevant energy scales in many systems, such as the excitonic molecule energy scale in semiconductors. Combining THz-TDS with optical excitation one can measure the evolution of optically induced changes in the real and imaginary part of the dielectric function with a probe energy much closer to the relevant energy scale in the material.

A typical example of mid-infrared reflectivity spectra calculated by M. Nagai *et all* is displayed in figure 3.18. The reflectivity has a very distinctive response in the case of different concentrations and spatial distributions of the photoexcited carriers: it is flat for a low density of carriers (situation (1)); it has a Drude like shape for a high carrier density uniformly distributed over the sample (situation (2)) and it displays a resonance for a high density of carriers, gathered in ”droplets” inhomogeneously distributed throughout

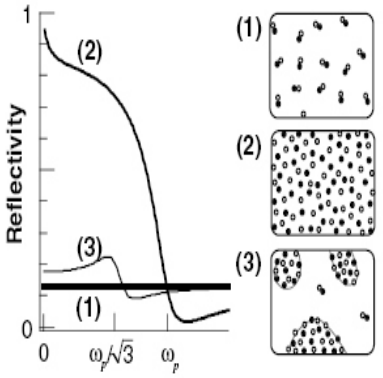

Figure 3.18: Typical response from different spatial distributions of photoexcited carriers in mid infrared pump-probe experiment. Reflectivity around plasma frequency $\hbar\omega_p$ at different distributions of electron-hole: (1) dilute excitonic gas, (2) homogenous plasma, and (3) electron-hole droplet. Reproduced from [32], with permission

the sample. This example demonstrates the possibility of using optical-pump THz-probe spectroscopy in order to induce and see the signature of a metal to insulator transitions for example: in the case of a metal one would see a Drude like sample response, while in the case of an insulator a flat response will be observed.

A time-resolved optical-pump THz-probe experimental setup is shown in fig. 3.19. In this setup please be aware that parabolic mirrors 1 and 3 were not well oriented (see the remarks about wrong paraboloids orientation made on page 53).

An intense optical pump pulse, which is derived from the same laser beam that triggers the THz transmitter and detector, photoexcites the sample. Using a mechanical delay line, the optically induced changes in the transmitted electric field can be measured with subpicosecond resolution. The complex sample signal as a function of frequency and pump-probe delay time τ is given by

$$S(\omega,\tau) = \frac{FFT(E_{eq}(t) + \Delta E(t,\tau))}{FFT(E_{ref}(t))} = \frac{E_{sig}(\omega,\tau)}{E_{ref(\omega)}} \tag{3.51}$$

where $E_{eq}(t)$ is the equilibrium scan of the sample in the time-domain without optical excitation, $\Delta E(t,\tau) = E_{ex}(t,\tau) - E_{eq}(t)$ is the induced change in the electric field with $E_{ex}(t,\tau)$ the scan of the sample with optical excitation.

Experimentally, $\Delta E(t, \tau = \tau_i)$ is obtained by scanning the THz probe delay line

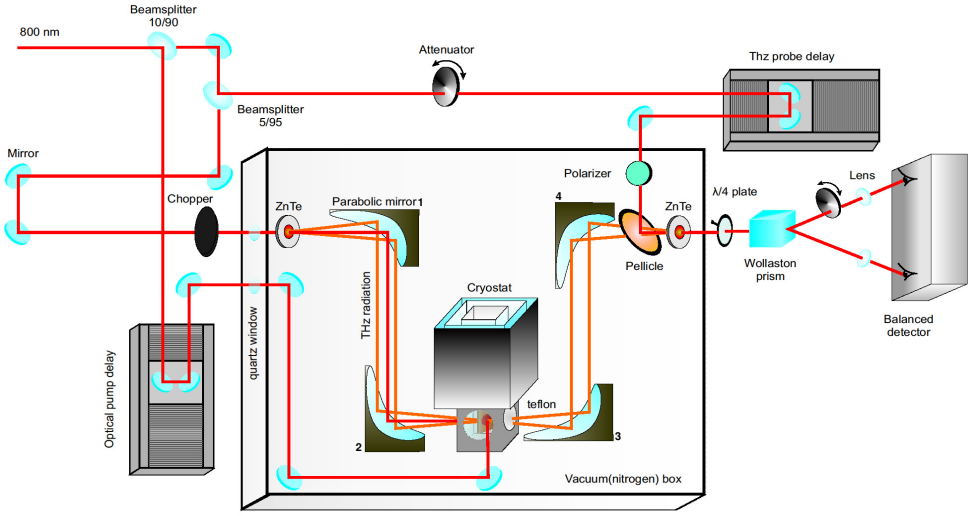

Figure 3.19: Typical optical setup in an optical-pump THz-probe experiment. An optical pump pulse directly excites the sample, and the focused THz beam probes the far-infrared properties of the sample as a function of time after optical excitation. Keep in mind that paraboloids 1 and 3 are not well oriented.

and mechanically chopping the optical pump delay line which is positioned at a specific pump-probe delay time $\tau = \tau_i$. This procedure measures the difference between $E_{ex}(t, \tau = \tau_i)$ and $E_{eq}(t)$ at the rate of the chopper frequency immediately yielding $\Delta E(t_r, \tau = \tau_i)$ at each THz probe delay time t_r. Alternatively, by chopping and scanning the THz probe delay line one would collect the data for $E_{ex}(t, \tau = \tau_i)$ (i.e. pump on) and $E_{eq}(t)$ (i.e. pump off) in separate scans. The direct measurement of $\Delta E(t, \tau)$ allows for increased signal sensitivity as it is more robust to system drift, particularly when the induced change is small. Then the real and imaginary part of the dielectric function can be obtained through a procedure which was given in the previous section. After obtaining $\Delta E(t, \tau = \tau_i)$, $E_{eq}(t)$ and $E_{ref}(t)$ are measured by chopping and scanning the THz probe delay line. $\Delta E(t, \tau = \tau_i)$ must be measured at each pump-probe delay time because the optical excitation can induce changes in both the phase and amplitude of the THz field.

However, for samples in which the optical excitation produces changes primarily in the amplitude of the THz electric field, an alternative method can be used. $\Delta E(t = t_{peak}, \tau)$ as a function of τ is obtained in a single scan by chopping and scanning the optical pump delay line while the THz delay line is positioned at the peak of the THz electric field. This method, if applicable, can provide considerable time savings in measuring the induced dynamics. It must be kept in mind that this procedure is an approximation which can be employed only when the induced change is small, or when the phase of the THz pulse does not change with optical excitation. This method is in most of the cases not applicable, because these requirements are only seldom met.

Time $\tau = 0$ is chosen as the pump pulse delay where a induced change in THz pulse amplitude is first observed. The THz electric field is four orders of magnitude lower than the excitation pulse electric field. Therefore, one can be sure that the THz pulse acts as a true probe pulse, not perturbing the system. One of the advantages of the THz-TDS is the distinctive detection method [47, 48]: both, the change in absorbance and the phase shift of all frequency components contained in the probe field are determined. This information can also be expressed in terms of complex conductivity spectrum $\sigma(\omega, \tau) = \sigma'(\omega, \tau) + i\sigma''(\omega, \tau)$, which is a function of the time τ after photoexcitation. The experimentally determined absorption and phase shift of the THz electric field $\Delta E(t, \tau)$ fully determine $\sigma(\omega, \tau)$ [49]. However, when $\sigma(\omega, \tau)$ changes on a time scale τ which is comparable or shorter with the THz pulse duration, the extraction of $\sigma(\omega, \tau)$ from $\Delta E(t, \tau)$ becomes more problematic, because the sample characteristics will be different between the beginnng and the end of the [39,49,50]. This effect must be taken into account in the data analysis. In the next section we will follow the same type of analyze performed by E. Hendry [50] and J.T. Kindt [49] when the sample properties are changing on a time scale comparable with the THz pulse time duration. It is better to consider in a first step the case of a time-independent carrier density of the sample, as shown in fig. 3.20(a). In this situation, the extraction of $\sigma(\omega, \tau)$ from the experimental data is straightforward when $\sigma(\omega, \tau)$ varies slowly in time τ, during the THz probe pulse (which has a main period of about 2 ps), because this allows the definition of a quasi-steady-state conductivity $\sigma(\omega)$ [47, 51, 52]. Before taking into account the THz field used in experiments, we evaluate the impulse-response current $j(t)$ after an extremely short pulsed field $E(t) = \delta(t - t')$ [53]. The impulse-response current can then be written as a product

$$j(t) = N j_0(t) \tag{3.52}$$

where $j_0(t)$ is the single particle current-response function and N is the number of (photoexcited) charge carriers [53]. $\sigma(\omega)$, the sample conductivity spectrum, is evaluated as the Fourier transform of $j(t)$. When the number of photoexcited charge carriers N is not time dependent, as in this steady state approximation, $j(t)$ is proportional to $j_0(t)$, which

decreases in time after the impulse $\delta(t-t')$ (see fig. 3.20(a)). The integration

$$J(t) = N\int_{-\infty}^{\infty} E_0(t')j_0(t-t')dt'. \tag{3.53}$$

will then give the total current generated by an arbitrary THz pulse $E_0(t)$. $J(t)$ can also be written as a convolution between the time-independent THz field and the impulse-response current:

$$J(t) = NE_0(t) * j_0(t). \tag{3.54}$$

Experimentally, the change in the transmitted THz field $\Delta E(t)$, due to photoexcitation is measured. If the sample excitation thickness is z_{slab} and the surrounding medium has the refractive index n_{THz}, from the Maxwell equations one can derive a relation which relates $\Delta E(t)$ and $J(t)$ [56]:

$$\Delta E(t) = -\frac{z_{slab}}{2\varepsilon_0 c n_{THz}} J(t) \tag{3.55}$$

However, this solution is applicable only for nondispersive sample and the photoinduced change in the THz electric field is much smaller that this field $\Delta E(t) \ll E(t)$. Taking into account the Fourier transforms of the last two equations, the conductivity spectrum $\sigma(\omega)$ in this steady-state approximation can be obtained:

$$\sigma(\omega) = -\frac{2\varepsilon_0 c n_{THz}}{z_{slab}} \frac{\Delta E(\omega)}{E(\omega)}. \tag{3.56}$$

In the last equation $E(\omega)$ and $\Delta E(\omega)$ are the Fourier transforms of the experimental data $E(t)$ and $\Delta E(t)$. The above approach can be effective only when the charge carrier concentration N does not change significantly over the duration of the THz pulse (~ 2 ps).

One can consider now the case of a nonsteady-state. The non-steady state is valid when the sample properties are changing fast: during the excitation, when the charge carriers are trapped fast or undergo recombination, or when the charges response changes in time. In this situation one would like to extract a time-dependent conductivity $\sigma(\omega, \tau)$ [49], but the extraction of this quantity which is varying with frequency and pump-probe time in not trivial. In the case of an infinitely short probe field $\delta(t-t')$, the formalism can be easily reconsidered for a density $N(t+\tau)$ decaying monotonously and simultaneously in the positive direction for both t and τ. In this case, we need to take into account the faster decay of current in the temporal region from t' to t (fig. 3.20(b)), because changes after t' affect the experimental signal, since carriers that decay can no longer contribute to the current at time t. The contribution of $N(t+\tau)$ to the current at time t is indicated by a black dot in fig. 3.20(b). Expanding this consideration for a density decaying monotonously across an arbitrary THz pulse shape, one can rewrite eq. (3.54) for decreasing density:

$$J(t) = N(t,\tau)[E_0(t) * j_0(t)]. \tag{3.57}$$

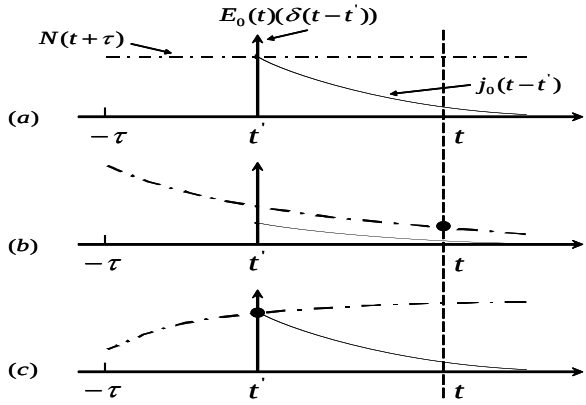

Figure 3.20: Evaluation of $j_0(t-t')$ (continuous light line) for the impulse by the THz field (depicted here as a delta function field $\delta(t-t')$). At a time t (vertical black, long dashed line) after excitation, $J(\tau,t,t')$ can be separated into an amplitude function $N(t+\tau)$ (dash point line) which represents the amplitude dependence of the pump delay $(t+\tau)$, and the average response of a single-particle to the impulse field, $j_0(t-t')$. (a) When the conductivity does not depend of the pump-probe delay, $N(t+\tau)$ does not change in time and the current at time t can be expressed as $J(\tau,t,t') = N\,j_0(t-t')$. (b) When the conductivity decreases with pump-probe delay, $J(\tau,t,t') = N(t+\tau)\,j_0(t-t')$ because, only the contribution of the remaining particles at time t (represented as a black dot) is to be considered. (c) When the conductivity is increasing with pump-probe delay, $J(\tau,t,t')$ is amplitude dependent at time t' (at the time of the impulse, represented here as a black dot), since any additional change in amplitude at later times is not affected by the impulse field $\delta(t-t')$. In this situation, the current density at time t can be written as $J(\tau,t,t') = N(t'+\tau)\,j_0(t-t')$. This figure is reproduced from [50], with permission.

An optical-pump THz-probe experiment on Cu_2O reveals that the optical excitation induces changes in both, the phase and amplitude of the THz field. In this situation, as discussed in the beginning of this section, $\Delta E(t,\tau)$ must be measured at each pump-probe delay. Figure 3.21 presents a schematic representation of the two dimensional

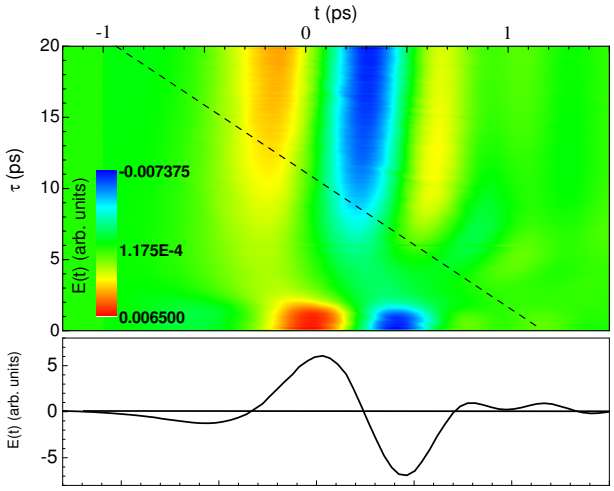

Figure 3.21: A measurement taken on a copper oxide sample. In the bottom part is the THz pulse before the arrival of the excitation pulse. The top plot represents the the THz pulses $E(t,\tau)$ at different times τ after the excitation. A decrease in the amplitude of $E(t,\tau)$ with τ is observed, indicating a decrease in conductivity with the pump-probe delay. There is also a shift of the waveform to the left. The dashed line at a 45^0 angle represents the path of the pump pulse in the measurement: each point in a horizontal cross section $E(t)$ has a different pump-probe delay. Transforming the data along this line introduces an alternative time τ' to describe the delay between the excitation pulse and all points on the probe THz pulse with the same pump delay.

analysis performed on the measured Cu_2O data. In the bottom part is the THz pulse before the arrival of the excitation pulse. The top plot represents the the THz pulses $E(t,\tau)$ at different times τ after the excitation. A decrease in the amplitude of $E(t,\tau)$ with τ is observed, indicating a decrease in conductivity with the pump-probe delay. There is also a shift of the waveform to smaller t. The dashed line at a 45^0 angle represents the path of the pump pulse in the measurement: each point in a horizontal cross section $E(t)$ has a different pump-probe delay. Transforming the data along this line introduces an alternative time τ' to describe the delay between the excitation pulse and all points on the probe THz pulse with the same pump delay.

The time-dependent conductivity can be extracted from the data, using a method introduced by Schmuttenmaer *et. all* [39, 49]. Before Fourier transforming the time-

domain data, we apply the transformation $\tau' = t + \tau$ to the last equation and obtain:

$$J_{proj}(t, \tau') = N(\tau')[E_0(t) * j_0(t)]. \tag{3.58}$$

The experimental data are transformed along the path of the excitation pulse (depicted as a dashed line in fig. 3.21). The points on a horizontal cross section of ΔE_{THz} are now at the same pump-probe delay. Eq. (3.55) for the case of time-dependent density will read:

$$\Delta E_{proj}(t, \tau') = -\frac{z_{slab}}{2\varepsilon_0 c n_{THz}} J_{proj}(t, \tau') \tag{3.59}$$

Considering the Fourier transforms of eqs. (3.58) and (3.59), the conductivity spectrum $\sigma(\omega, \tau')$ can then be calculated

$$\sigma_{proj}(\omega, \tau') = -\frac{2\varepsilon_0 c n_{THz}}{z_{slab}} \frac{\Delta E(\omega)}{E(\omega, \tau')}. \tag{3.60}$$

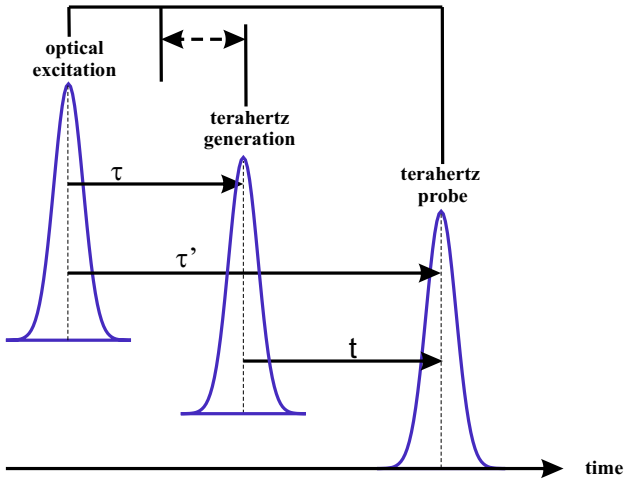

Figure 3.22: Pulses which are used during an optical-pump terahertz-probe experiment and the time delays between them. The time delays have the same notations as in the 2D data processing section.

The decay of the charge-carrier population represents the dependence of the pump-probe delay τ'. The response of an infinitely long-lived charge carrier is represented in the frequency-dependent part. The new charge carriers which might be created during or after the THz pulse are not taken into account in eqs. (3.57) to (3.60). This situation can be easily depicted considering a delta function probe field $\delta(t - t')$ (see fig. 3.20(c)).

When the density is increasing between t' and t, the additional charges are not probed by the field at time t' and they do not result in a current increase at time t. The current can then be calculated using $N(t' + \tau)$ instead of $N(t + \tau)$. It must be noted that introducing a t' dependence in N means that the equivalent form of eq. (3.57) for increasing density is not a simple convolution and the interpretation of the extracted conductivity spectrum is not direct. In other words the transformation we apply to the data in this section does not give reliable results when the pump and THz pulse overlap. For this reason we do not use during analyze data taken at pump-THz delays smaller than 3 ps.

An alternative to the two dimensional data analyze described above is to experimentally make sure that the delay between the optical excitation pulse and the THz probe pulse remains constant during the THz pulse measurement. This would significantly shorten the data analysis process, as well as the time duration of the measurement itself.

In a classical optical-pump, terahertz-probe experimental setup, two delay stages are used. One of them, usually placed on the terahertz probe beam is varying the delay between the terahertz probe beam and the terahertz generation pulse (time t in our notation, see fig. 3.22). The second delay, usually placed on the optical excitation pulse, is varying the time between the terahertz generation pulse and the optical excitation pulse (time τ in our notation). There is a possibility to perform the THz measurements keeping the delay between the optical-pump pulse and the terahertz probe pulse, τ', constant, while moving them both relative to the terahertz generation pulse (in fig. 3.22, this movement is represented by a dashed line). This possibility does not require any change in the classical setup. Without changing the setup, one can simply move simultaneously both delay stages with the same speed during the THz pulse measurement. This will ensure a constant τ'.

References

[1] A. Gurtler, C. Winnewisser, H. Helm and P. Uhd Jepsen, J. Opt. Soc. Am. A, **17**, 74 (2000).

[2] A. J. Taylor, P. K. Benicewicz and S. M. Young, Opt. Lett., **18**, 1340 (1993).

[3] J. C. Diels and W. Rudolph, *Ultrashort Laser Pulse Phenomena: Fundamentals, Technique and Applications on a Femtosecond Time Scale*, (Academic Press, San Diego - London, 1995).

[4] A. Yariv, *Quantum Electronics, 3rd Edition*, John Wiley and Sons, Ney York, 1988).

[5] Y. R. Shen, *The principles of Nonlinear Optics*, (John Wiley and Sons, New York, 1984).

[6] P. R. Smith and D. H. Auston and M. C. Nuss, IEEE J. Quantum Electron, **24**, 255 (1988).

[7] C. Ludwig and J. Kuhl, Appl. Phys. Lett., **69**, 1194 (1996).

[8] J. T. Kindt and C. A. Schmuttenmaer, J. Phys. Chem., **100**, 10373 (1996).

[9] L. Xu and X. C. Zhang and D. H. Auston and B. Jalali, Appl. Phys. Lett., **59**, 3357 (1991).

[10] X. C. Zhang and D. H. Auston, J. Electromagn. Waves Appl., **6**, 85(1992).

[11] B. B. Hu and A. S. Weling and D. H. Auston and A. V. Kuznetsov and C. J. Stanton, J. Electromagn. Waves Appl., **49**, 2234 (1994).

[12] X. C. Zhang, B. B. Hu, J. T. Darrow and D. H. Auston, Appl. Phys. Lett., **56**, 1011 (1990).

[13] D. You, R. R. Jones, P. H. Bucksbaum and D. R. Dykaar, Opt. Lett., **18**, 290 (1993).

[14] H. Hamster and A. Sullivan and S. Gordon and W. White and R. W. Falcone, Phys. Rev. Lett., **71**, 2725 (1993).

[15] D. J. Cook and R. M. Hochstrasser, Opt. Lett., **25**, 1210 (2000).

[16] Q. Chen and Z. P. Jiang and M. Tani and X. C. Zhang, Electron. Lett., **36**, 1298 (2000).

[17] M. Tani and Z. P. Jiang and X. C. Zhang, Electron. Lett., **36**, 804 (2000).

[18] P. Y. Han and M. Tani and F. Pan and X. C. Zhang, Opt. Lett., **25**, 675 (2000).

[19] J. J. Carey and R. T. Bailey and D. Pugh and J. N. Sherwood and F. R. Cruickshank and K. Wynne, Appl. Phys. Lett., **81**, 4335 (2002).

[20] C. Winnewisser, *Electrooptische Detektion von ultrakurzen elektromagnetischen Pulsen*, (Phd thesis, University of Freiburg, Germany, 1999).

[21] R. K. Ram and S. S. Kuswaha and J. S. Rajput, J. Phys. Soc. Jpn., **58**, 4032(1989).

[22] C. Kubler, R. Huber, S. Tubel and A. Leitenstorfer, Appl. Phys. Lett., **85**, 3360 (2004).

[23] P. Y. Han and X. C. Zhang, J. Electromagn. Waves Appl., **73**, 3049 (1998).

[24] K. Reimann and R. P. Smith and A. M. Weiner and T. Elsasser and M. Woerner, Opt. Lett., **28**, 471 (2003).

[25] Gregor H. Welsh, Neil T. Hunt, and Klaas Wynne, Phys. Rev. Lett., **98**, 026803 (2007).

[26] X. Xin, H. Altan, A. Saint, D. Matten, and R. R. Alfano, J. of Appl. Phys., **100**, 094905 (2006).

[27] P. Y. Han and G. C. Cho and X. C. Zhang, J. Nonlinear Opt. Phys. Mater, **8**, 89 (1999).

[28] P. Uhd Jepsen and R. H. Jacobsen and S. R. Keiding, J. Opt. Soc. Am. B, **13**, 2424 (1996).

[29] H. P. Wagner and M. Kuhnelt and W. Langbein and J. M. Hvam, Phys. Rev. B, **58**, 10494 (1998).

[30] A. Shimizu and M. Yamanishi, Phys. Rev. Lett., **72**, 3343(1994).

[31] P. Uhd Jepsen and B. M. Fischer, Opt. Lett., **30**, 29 (1993).

[32] M. Nagai, R. Shimano, and M. K. Gonokami, Phys. Rev. Lett., **86**, 5795 (2001).

[33] Z. P. Jiang and X. C. Zhang, Opt. Lett., **23**, 1114 (1998).

[34] P. Uhd Jepsen and Z. P. Jiang and X. C. Zhang, Appl. Phys. Lett., **72**, 1945 (1998).

[35] P. Uhd Jepsen and F. G. Sun, Z. P. Jiang and X. C. Zhang, Appl. Phys. Lett., **73**, 2233 (1998).

[36] P. Uhd Jepsen and J. Shan, A. S. Weling, E. Knoesel, L. Bartels, M. Bonn, A. Nahata, G. A. Reider and T. F. Heinz, Opt. Lett., **25**, 426 (2000).

[37] P. Uhd Jepsen and A. Nahata and T. F. Heinz, Opt. Lett., **23**, 67 (1998).

[38] Q. Chen and X. C. Zhang, Appl. Phys. Lett., **74**, 3435 (1999).

[39] M. C. Beard, G. M. Turner and C. A. Schmuttenmaer, Phys. Rev. B, **62**, 15764 (2000).

[40] A. Nahata, D. H. Auston and T. F. Heinz, Appl. Phys. Lett., **68**, 150 (1996).

[41] B. E. A. Saleh and M. C. Teich, *Fundamentals of photonics*, (John Wilez and Sons, Inc., New York, 1991).

[42] H. Selig, *Electro-optisches Sampling von Terahertz-Pulsen*, (Diploma thesis, Universitat Hamburg, Germany, 2000).

[43] A. Nahata, A. S. Weling and T. F. Heinz, Appl. Phys. Lett., **69**, 2321 (1996).

[44] K. H. Yang, P. L. Richards and Y. R. Shen, Appl. Phys. Lett., **19**, 285 (1971).

[45] Q. Wu, M. Litz and X. C. Zhang, Appl. Phys. Lett., **68**, 2924 (1996).

[46] P. Uhd Jepsen, C. Winnewisser, M. Schall, V. Schyja, S. R. Keyding and H. Helm, Phys. rev. E, **53**, R3052 (1996).

[47] M. C. Beard, G. M. Turner, and C. A. Schmuttenmaer, J. Phys. Chem. B **106**, 7146 (2002).

[48] G. Gallot and D. Gischkowsky, J. Opt. Soc. Am. B **16**, 1204 (1999).

[49] J. T. Kindt and C. A. Schmuttenmaer, J. Chem. Phys. **110**, 8589 (1999).

[50] E. Hendry, M. Koeberg, J. M. Schins, H. K. Nienhuys, V. Sundstrom, L. D. A. Siebbeles, and M. Bonn , Phys. Rev. **B 71**, 125201 (2005).

[51] J. Shan, F. Wang, E. Knoesel, and T. F. Heinz, Phys. Rev. Lett. **90**, 247401 (2003).

[52] E. Knoesel, M. Bonn, J. Shan, F. Wang, and T. F. Heinz, J. Chem. Phys. **121**, 394 (2004).

[53] N. V. Smith, Phys. Rev. B, **64**, 155106 (2001).

[54] E. Hendry, J. M. Schins, L. P. Candeias, L. D. A. Siebbeles, and M. Bonn, Phys. Rev. Lett., **92**, 196601 (2004).

[55] M. C. Beard, and C. A. Schmuttenmaer, J. Chem. Phys., **114**, 2903 (2001).

[56] H. K. Nienhuys and V. Sundstrom, Phys. Rev. B, **71**, 235110 (2005).